Check for updates

ADVANCED MATERIALS TECHNOLOGIES
www.advmattechnol.de

An All-MXene-Based Flexible, Seamless System with Integrated Wireless Charging Coil, Micro-Supercapacitor, and Photodetector

Zhongyi Duan, Chuqiao Hu, Weijia Liu, Jinhai Liu, Zhengyu Chu, Weiqing Yang, La Li,* and Guozhen Shen**

Fabrication of miniature-integrated devices combining energy harvester, energy storage, and various sensors via simple, fast, and efficient ways is strongly desired for the practical application of integrated smart systems. Herein, this work presents a simple one-step laser scribing method to prepare an all MXene-based seamlessly integrated system with integrated wireless charging coil, micro-supercapacitor, and photodetector in a small area of only 1.78 cm^2. All the three modules in the integrated system are composed entirely of $Ti_3C_2T_x$ MXene and are connected with highly conductive MXene wires without additional welding or assembling operation. The energy is first received by the wireless charging coil and then stored in the Zn-ion micro-supercapacitor, which is subsequently used to drive the surface-modified (dodecyl triethoxysilane) DCTES-MXene-based photodetector, thus realizing the complete energy cycles. This work conceptually illustrates a simple method for designing and preparing integrated multifunctional wearable devices.

1. Introduction

With the increase in demand for Internet of Things (IoTs), miniaturized on-chip integrated and multifunctional devices that possess lightweight and flexible features have become increasingly important in developing wearable electronics that can be used in fields of implantable biosensors, human–machine interaction, and environment monitoring.[1–6] Generally, the on-chip integrated systems should consist of energy harvester, energy storage, and smart sensors connecting with conducting wires in a limited space. In order to construct integrated systems, a commonly used method is to use ambient energy, such as heat, wind, and solar to power the system in place of a bulky external power source.[7,8] However, these ambient energy sources suffer from the unstable discontinuous energy supply. Another frequently used method is wireless charging coil (WCC) which shows more stable and faster charging, making it widely used in intelligent electronic devices.[9–11] For example, Kim et al.[12] skillfully integrated a wireless charging antenna, capacitor, and intraocular pressure sensor into the contact lens to enable real-time intraocular pressure measurement using a smartphone. These systems adopted the contactless WCCs to avoid unnecessary external connections and realize high integration and miniaturization of devices. However, the individual functions of the integrated systems are usually based on different functional materials, which is hard to fabricate the integrated system in one fabrication technology and increases the complexity and unnecessary cost of integrated and miniaturized devices. Therefore, in order to realize a feasible fabrication of integrated devices, it is an effective method to use a single material as multiple parts.[13,14]

Recently, 2D transition metal carbides and nitrides called MXenes, which are generally obtained by selected etching MAX precursors, have been widely studied. They are generally credited as $M_{n+1}X_nT_x$ (n = 1–4), where M, X, and T are the early transition mental, carbon and/or nitrogen, and surface termination like hydroxyl (–OH), oxygen (=O), and fluorine (–F), respectively.[15,16] The elemental diversity and abundance of surface functional groups render MXenes excellent conductivity, adjustable chemistry, and electrochemical activity, making MXenes excellent candidates for supercapacitors, different types of sensors, lithium-ion battery, and electromagnetic interference shielding, etc.[17–22] Although Shao et al. recently innovatively combined MXene with wireless charging technology to verify the possibility of MXene as a wireless energy harvester, 3D printing technique is used, which imposes high requirements for equipment and ink preparation

Z. Duan, W. Yang
Key Laboratory of Advanced Technologies of Materials (Ministry of Education)
School of Materials Science and Engineering
Southwest Jiaotong University
610031 Chengdu, P. R. China
E-mail: wqyang@swjtu.edu.cn

C. Hu, W. Liu, L. Li, G. Shen
School of Integrated Circuits and Electronics
Beijing Institute of Technology
100081 Beijing, P. R. China
E-mail: lali@bit.edu.cn; gzshen@bit.edu.cn

J. Liu, Z. Chu
Beijing Circue Energy Technology Co., Ltd.
100085, No.6 Chuangye RD., ShangDi Information Industry Base Beijing, P. R. China

The ORCID identification number(s) for the author(s) of this article can be found under https://doi.org/10.1002/admt.202300157

DOI: 10.1002/admt.202300157

 © 2023 Wiley-VCH GmbH

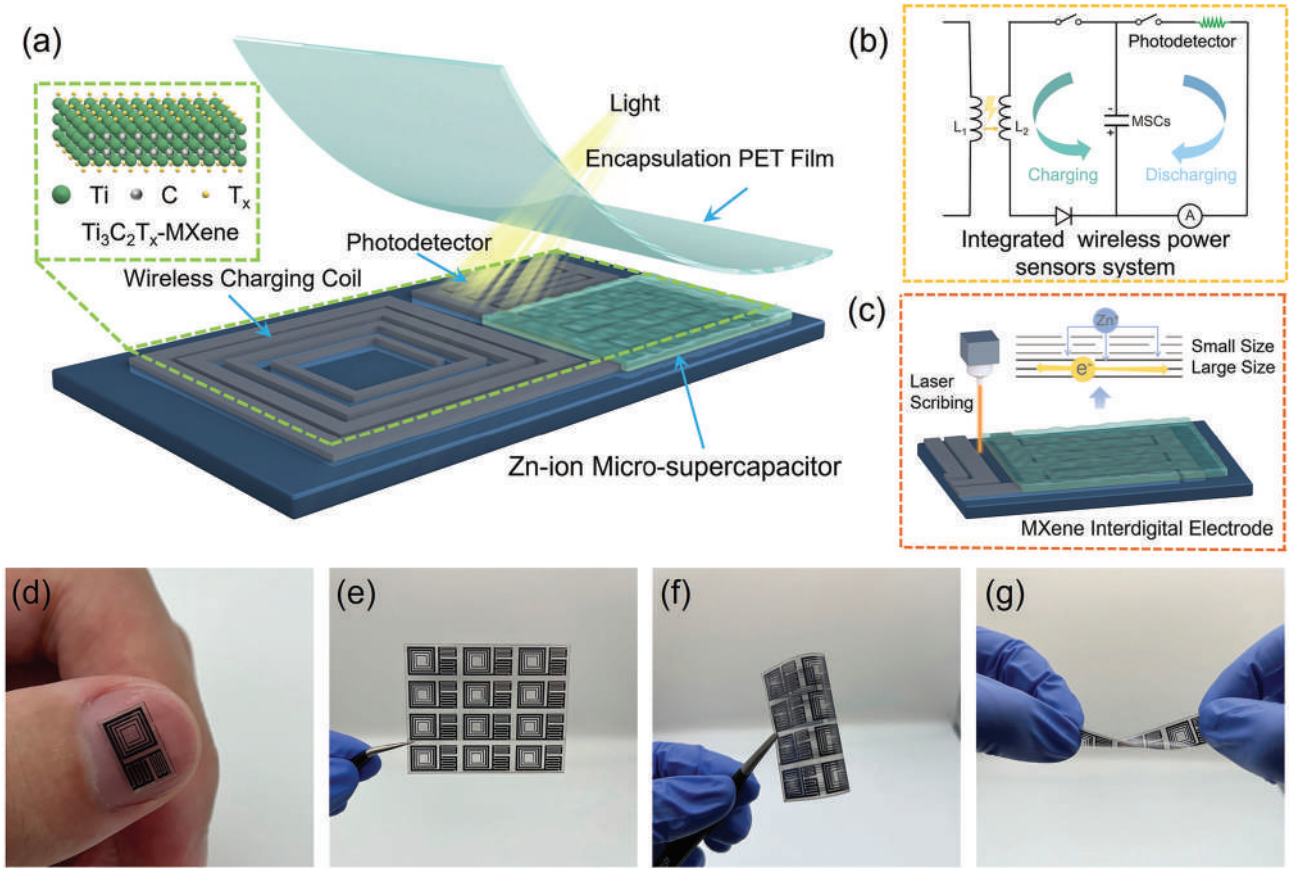

Figure 1. Schematic of the all-MXene-based integrated system. a) The system contains a WCC, a Zn-ion MSC, and a photodetector, all of which are composed of $Ti_3C_2T_x$-MXene. b) Schematic diagram of the integrated wireless power sensors system. c) Diagram of the 3D structure of MXene interdigital electrode. d) An optical image of the integrated system. e) Photograph of integrated devices arrays. f,g) Photograph of the integrated system under bending and distortion.

and requires post-treatments as well. Thus, developing simple, fast and low cost procedures is highly desirable. Compared to high-precision 3D printing technology, the mature laser etching technology has the advantages of fast processing speed, low cost and no complicated post-processing process. Based on the excellent properties of MXenes, in this work, we proposed a simple, one-step protocol to manufacture an all-MXene-based, seamlessly integrated system by laser scribing method. The integrated system is consisted of a WCC for energy transmission, a Zn-ion micro-supercapacitor (MSC) for energy storage, and an MXene-based photodetector for photoelectric detection, connecting with highly conductive MXene wires. The conductivity of the $Ti_3C_2T_x$ MXene was regulated during the synthesis process, where the large-sized $Ti_3C_2T_x$ MXene flakes served as conductive wires and WCC, while small-sized $Ti_3C_2T_x$ MXene flakes were utilized in the fabrication of MSCs (with an area capacitance of 84.07 mF cm^{-2} at a scan rate of 20 mV s^{-1}). More importantly, by adjusting the surface termination, the surface-modified (dodecyl triethoxysilane) DCTES-MXene as the photosensitive material realized the construction of a stable photodetector. As a result, the energy received by the WCC will be stored in the MSC and later drive the photodetector, avoiding external power supply and indicating the great potential for miniaturization of multifunctional integrated wearable devices.

2. Results and Discussion

The structure of the integrated system was presented in **Figure 1**a, consisting of three modules, a WCC, an MSC, and a photodetector. All three components are prepared via the one step laser scribing method with $Ti_3C_2T_x$-MXene acting as energy harvesting, energy storage, and light detection material as well as conductive wires in this system. First, the MXene dispersion was dropped to the treated PET substrate, which was obtained from selective etching in Ti_3AlC_2-MAX phase.[16] Subsequently, an additional layer of sonicated MXene was deposited in the MSC region. After sonication, the sheet size of MXene will be reduced, thus shorten the transmission path of electrolyte ions and provide active sites.[23,24] Then, the unwanted areas were removed using laser scribing technique to obtain the desired device structure.[25] No assembly and soldering operations were required between the three modules prepared by this one-step method, thus reducing the processing flow and difficulty and improving the stability of the integrated device. Further, a seamless device can avoid the damage caused by poor solder joints during the bending process. Finally, the surface-modified MXene was deposited on the interdigital electrodes to get photodetector.[26]

Due to its excellent electrical conductivity and abundant surface functional groups, MXene has been widely used in energy

© 2023 Wiley-VCH GmbH

2365709x, 2023, 15, Downloaded from https://onlinelibrary.wiley.com/doi/10.1002/admt.202300157 by du fu - Columbia University Libraries , Wiley Online Library on [07/09/2023]. See the Terms and Conditions (https://onlinelibrary.wiley.com/terms-and-conditions) on Wiley Online Library for rules of use; OA articles are governed by the applicable Creative Commons License

2365709x, 2023, 15, Downloaded from https://onlinelibrary.wiley.com/doi/10.1002/admt.202300157 by du fu - Columbia University Libraries , Wiley Online Library on [07/09/2023]. See the Terms and Conditions (https://onlinelibrary.wiley.com/terms-and-conditions) on Wiley Online Library for rules of use; OA articles are governed by the applicable Creative Commons License

storage and sensing applications, and it also has potential for energy harvesting.[18,27] In our fabricated system here, an antenna prepared by MXene was used as a WCC. According to Faraday's law of electromagnetic induction, when the secondary coil L_2, prepared by MXene, is in the changing magnetic field generated by alternating current in L_1, an induced current will be generated in the L_2 and achieve contactless transmission of energy (Figure 1b). The received energy will be stored in the MXene-based MSC and used as an internal power source to drive the photodetector, or other sensors, avoiding the need for external power wiring and enabling device integration. For performance enhancement concerns, the MSC electrode adopted a layered 3D structure on the microscopic scale. Small size nanosheets shorten the ion transport distance and were mainly used for energy storage, while large size nanosheets shorten the electron transport distance and acted as current collectors (Figure 1c).[23] Based on the excellent electrical conductivity of MXene, they were also directly used as current collectors for the photodetector instead of additional noble metals such as gold.[7] Then, on the laser-cut interdigital electrode, an additional layer of DCTES-MXene with -$C_{12}H_{26}$ functional groups grafted on the surface was dropped as a photosensitive material. Finally, due to the high precision of laser scribing technology, the entire integrated device occupies an area of only 1.78 cm^2, smaller than a fingernail (Figure 1d). Also, based on laser scribing process, the integrated device can be prepared in arrays as shown in Figure 1e. And due to the excellent flexibility of the PET substrate and MXene, the seamlessly integrated devices can be easily bent and twisted (Figure 1f,g).

In integrated systems, an energy storage device is often required to provide long-term stable energy output to functional sensors. Compared with batteries, MSCs have higher power density, making them suitable for combining with wireless charging for fast charging in a few minutes.[28] Since its discovery in 2011, MXene had been widely tried as an electrode for MSCs. To improve its electrochemical performance, one method is to chemical modify MXenes and/or assemble MXenes with active materials, such as graphene or carbon nanotubes.[15,20] However, these methods usually sacrificed the excellent conductivity of MXenes. Another method that was recently developed is to construct 3D structured electrode by using templates methods, 3D print technology, and so on. But these methods often involved complex procession techniques and post-treatment, thus greatly increased the difficulty of preparation.[21]

Recently, researchers found that by simply depositing small-sized MXene flakes onto large-sized MXene flak layer can efficiently improve the electrochemical performance of MXene-based supercapacitors,[23,24] because such a procedure preserved the excellent conductivity of large MXene layers while optimizing the performance of the MSC by shortening the electrolyte ion transport path (**Figure 2**a). Here, to achieve seamless integration with WCC and photodetector, in the MSC part, we also deposited additional small MXene sheets on top of the large MXene sheet layer. Figure 2b presents the compared cyclic voltammetry (CV) curves of three contrast supercapacitors, without/with small/large size MXene sheet beyond basal MXene layer, at the scan rate 20 mV s^{-1}. The results showed that the area-specific capacitance with the additional small size MXene layer is higher than that without the small size layer, with a 131.5% improvement (from 30.26 to 70.07 mF cm^{-2}). It is also 52.2% higher than the supercapacitors with an additional large size MXene layer (46.05 mF cm^{-2}), improved by an efficient ion transport path and a large number of defects and edges on small-size MXene as electrochemically active sites. In Figure S2 (Supporting Information), the dynamic light scattering (DLS) showed a reduction in the size of the MXene sheet after one hour of ultrasound, mainly distributed around 300 μm. Furthermore, the XRD pattern in Figure S3 (Supporting Information) showed that there was no significant difference between them. These results demonstrated that the supercapacitor capacity can be improved by optimizing the MXene sheet size, which optimizes the ion transport efficiency.

Figure 2c depicts the CV curves of our MSC at the scan rates from 5 to 200 mV s^{-1} at a constant potential window of 1.2 V. The CV curves presented a quasi-rectangular shape at low scan rates, corresponding to the electrical double layer capacitive behavior of $Ti_3C_2T_x$-MXene, and showed small humps during both the cathodic and anodic sweeps, which should be caused by the reversible interactions of hydronium ions and oxygen surface terminations. The galvanostatic charge/discharge (GCD) curves at various current densities rates, ranging from 0.1 to 1.0 mA cm^{-2}, were exhibited in Figure 2d. The typically triangular shape of the GCD curve revealed the reversible electric double layer capacitive behavior. The areal capacitances calculated from CV and GCD curves are 84.07 mF cm^{-2} at a scan rate of 20 mV s^{-1}, and 51.0 mF cm^{-2} at a current density of 0.1 mA cm^{-2}, respectively. And the areal capacitance of the present work was compared with other MXene based micro-supercapacitors in Table S1 (Supporting Information), the optimized electrodes showed a higher area specific capacitance. Meanwhile, Figure 2e demonstrates its good rate capability, maintaining 70.5% of the initial capacity at a current density of 1 mA cm^{-2}. Figure 2f depicts the electrochemical impedance spectra (EIS) of the MSC before and after cycles, showing low resistances of 68.62 and 80.52 Ω, respectively. The resistance of MSC was in the same order of magnitude with MSC using precious metals as current collectors, which further demonstrated the excellent electrical conductivity of large-sized MXene film (Table S1, Supporting Information). Owing to the flexibility of the PET substrate and $Ti_3C_2T_x$-MXene, the MSC had good flexibility with no obvious capacity decay after bending 180° (Figure 2g). Also, the MSC demonstrated a good cycle stability, maintaining 95% capacitance after 10 000 charge/discharge cycles (Figure S4, Supporting Information). In addition, the comparison of energy and power densities of the device with other types of MSCs was plotted in the Ragone plot in Figure 2h. The largest areal energy density obtained by the optimized MSCwas about 16.814 μWh cm^{-2} at a power density of 252.21 μW cm^{-2}, which is almost ten times more than that of MXene@rGO MSCs (1.6 μWh cm^{-2}, 70 μW cm^{-2}).[24,29–32] Overall, the energy and power density of MSCs can be effectively enhanced by tuning the size of the nanosheets and optimizing the ion transport paths, indicating a broad potential for applications in integrated devices.

Based on the MXene's excellent electrical conductivity, a WCC was designed and fabricated for charging the integrated system. To get optimized performance, we carefully tuned the structure of the WCC by balancing the miniaturization and lightweight considerations. For wireless charging technology, there are usually three loss mechanisms: substrate loss, skin effect, and proximity effect.[33] In our designed integrated system, an insulated PET is

 © 2023 Wiley-VCH GmbH

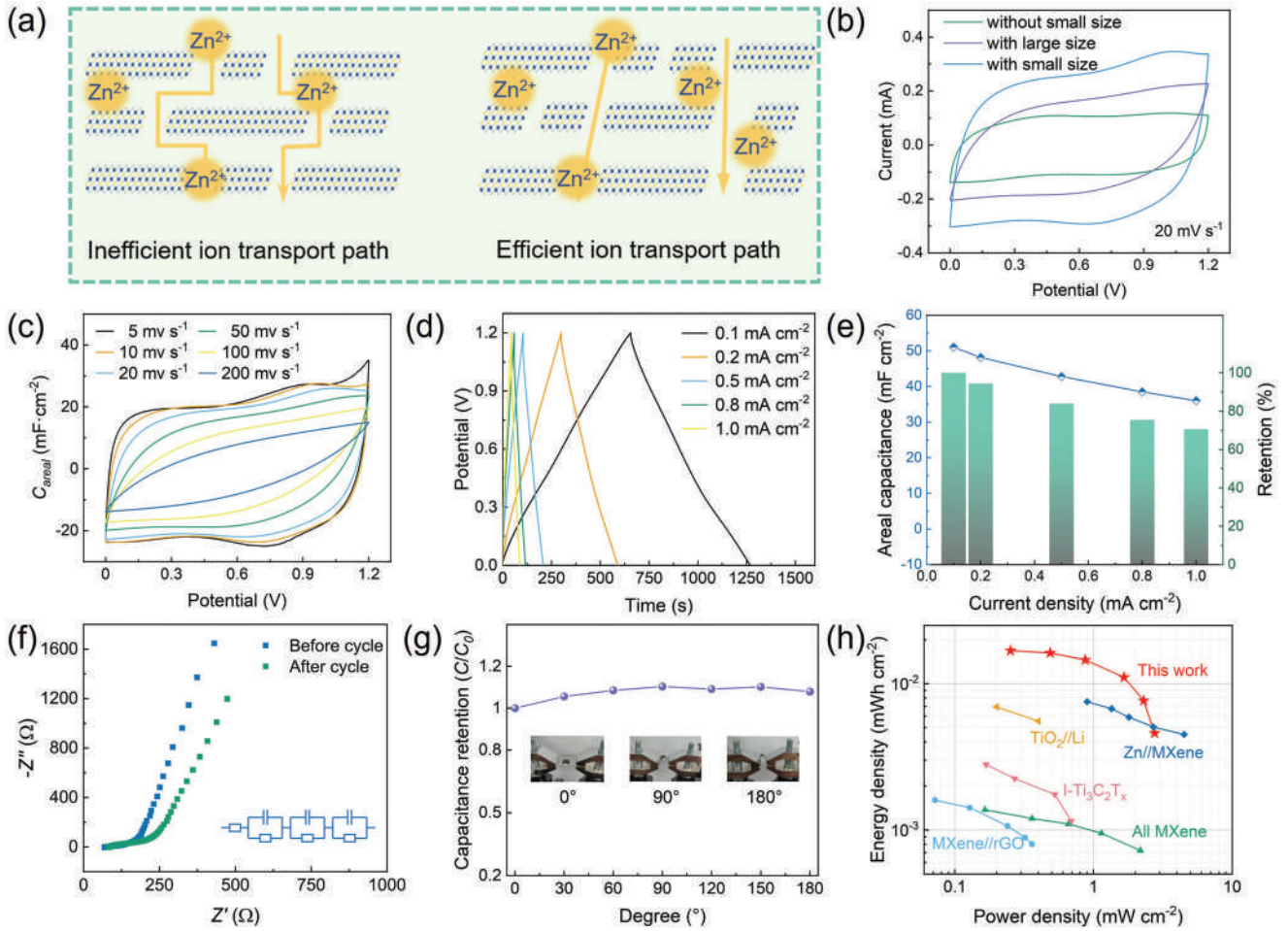

Figure 2. Electrochemical performance of the Zn-ion MSC. a) Illustration of ion transport path. b) Comparison of CV curves for the three cases, without/with small/large size MXene sheet beyond basal MXene layer, at the scan rate 20 mV s^{-1}. c) CV curves of MSC at the scan rates from 5 to 200 mV s^{-1} at a constant potential window of 1.2 V. d) GCD curves at various current densities, from 0.1 to 1.0 mA cm^{-2}. e) Variation of areal capacitance with various current densities. f) The Nyquist impedance plot of the MSC before and after cycles. g) Capacitance retention of the MSC at different bending states. The insets are the corresponding digital photos of the MSC under bending. h) Comparative areal energy and power densities (Ragone plot) of the MSC with different electrode materials.

used as substrate with almost no substrate loss. Due to its thinness and low operating frequency, the energy loss from the skin effect in the planar WCC is also negligible. Thus, subsequently, the impact of the proximity effect was mainly considered to tuning the performance of the WCC. The proximity effect refers to the interaction of the magnetic fields generated by adjacent wires in an energized coil, thus changing the current distribution inside the wire and manifesting as an increase in wire resistance. In a typical coil magnetic field, the magnetic field strength gradually increases from the outer to the inner circle, which in turn caused an increase of the proximity effect in the inner circle. Therefore, a reasonable coil structure design is desired to get optimized performance.

To investigate the performance of our MXene-based WCC, we designed two WCC structures, the fixed WCC (F-WCC) and the gradually changed (G-WCC), as shown in Figure S5 (Supporting Information). For both structures, the outer opening diameter (D_{out}) and the sum of line width and spacing (S_{ws}) remained the same. Besides, to maximize chip area utilization and reduce processing difficulties, square coils were adopted in both structures as well. **Figure 3**a,b shows the magnetic field distribution during the wireless power transmission. The magnetic field acted as a medium for energy exchange. When the alternating current through the primary coil generates an alternating magnetic field, a current in the secondary coil will be generated, thus enabling contactless energy transfer in the air. From the figures, it can be seen that the magnetic field strength in the center part of the primary and secondary coils was much higher than the edge region, resulting in a dominant proximity effect at the center of the coil. Compared with antenna surface current distribution at 100 kHz (Figure 3c,d), G-WWC presented a uniform current distribution. On the contrary, the current distribution of F-WCC was concentrated on the center of wire, especially in the inner circles. Besides, from Figure 3e,f, we can see that the ohmic loss of G-WCC was better than F-WCC, which will reduce heat generation during power transmission. This can be attributed to the structural design of the G-WCC: the narrower lines will increase line spacing and reduce the proximity effect in the coil center, where

© 2023 Wiley-VCH GmbH

2365709x, 2023, 15, Downloaded from https://onlinelibrary.wiley.com/doi/10.1002/admt.202300157 by du fu - Columbia University Libraries , Wiley Online Library on [07/09/2023]. See the Terms and Conditions (https://onlinelibrary.wiley.com/terms-and-conditions) on Wiley Online Library for rules of use; OA articles are governed by the applicable Creative Commons License

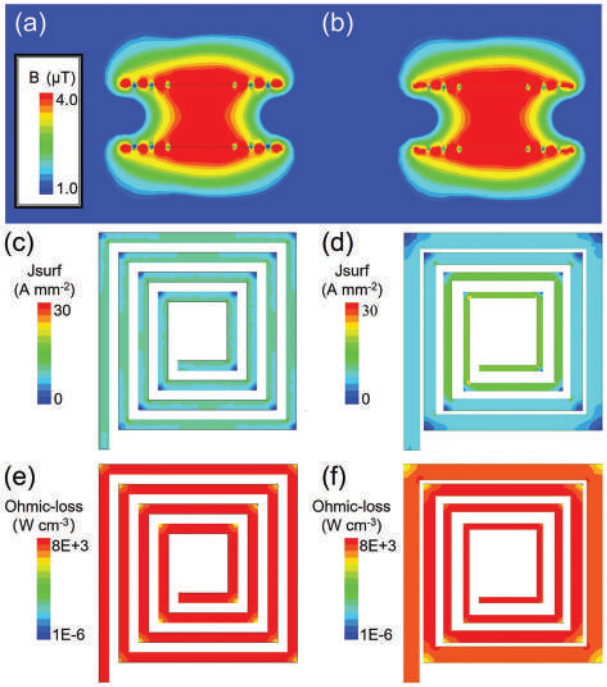

Figure 3. Simulation of the MXene-based WCC. a,b) Magnetic field distribution between the primary and secondary coils. c,d) Surface current distribution of the MXene-based WCC at 100 kHz. e,f) Ohmic loss of the MXene-based WCC.

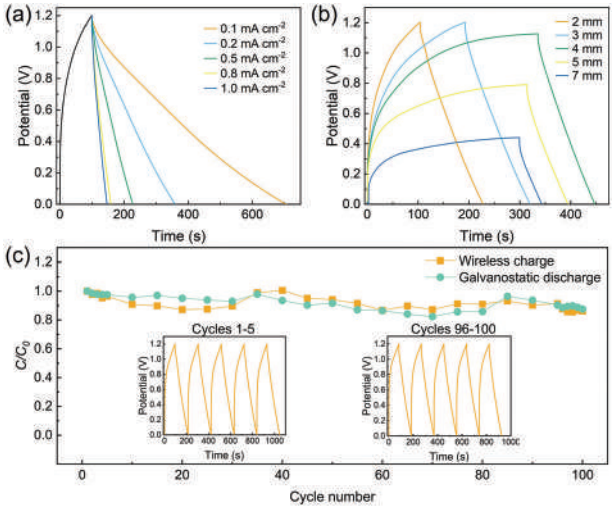

Figure 4. Characterization of the wireless charging system. a) The curves of the wireless charging with a transmission distance of 2 mm between the WCC, and galvanostatic discharging at various current densities. b) The dependence of this wireless charging/galvanostatic discharging characteristic on the transmission distance (from 2 to 7 mm). c) The cyclic performance of this wireless charging/galvanostatic discharging capability of the integrated WCC-MSC system.

the magnetic field is stronger, and inversely the wider lines at the coil edge will reduce the ohmic loss. Based on these simulation results, we confirmed that the design and optimization of the structure of WCCs will definitely improve their performance, and potentially the MXene-based WCCs can be used in areas such as medical implantable electronics and integrated sensing.

Based on the optimization of MXene-based WCC and MSC, the charging and discharging capability of the wireless charging system was further investigated. For this test, a commercial WCC was used as the transmitter, the optimized WCC was used as the receiver. To achieve a stable charging process, a rectifier diode (1N4148) was applied between the WCC and MSC to convert alternating current into direct current.[34] **Figure 4**a depicts the curves of the wireless charging and galvanostatic discharging at various current densities with a transmission distance of 2 mm between the WCC. With wireless charging, the supercapacitor can be fully charged in 2 min (black line). Compared with the GCD curves in Figure 3d, the current density in this wireless charging state was expected to be ≈0.5 mA cm^{-2}. Figure 4b presents the dependence of the wireless charging/galvanostatic discharging characteristic on the transmission distance (from 2 to 7 mm), and the MSC could be charged completely when the distance was about 4 mm. When the distance increased above this threshold, the wireless charging/galvanostatic discharging performance was obviously degraded. This was because the wireless charging mechanism follows the principles of Electromagnetic Induction, realizing the conversion between magnetic field energy and electrical energy. As the distance increased, the strength of the magnetic field decreased. Figure 4c presents the cyclic performance of the wireless charging/galvanostatic discharging capability of the integrated WCC-MSC system at the gap distance of 2 mm. The insets showed the wireless charging/galvanostatic discharging curves of five cycles before and after, respectively, and no obvious changes were observed after 100 cycles. Meanwhile, the capacity still remained around 90% after 100 cycles. These results showed that the optimized integrated WCC-MSC system can provide reliable energy conversion and storage performance, which indicated its substantial application potential in integrated devices.

The excellent performance of integrated wireless charging MSC endows them with the ability to be applied in practical highly integrated electronics, which combine energy transmission, energy storage, and sensing. **Figure 5**a shows the process of wireless charging, realizing contactless power supply. In the upper right area, a photodetector was integrated into the device, while again using the highly conductive MXene as the current collector (Figure 5b). Surface-grafted MXenes with -$C_{12}H_{26}$ were selected as photosensitive material, and its preparation process was shown in Figure 5c (details can be found in the Experimental section).[25] $Ti_3C_2T_x$-MXene nanosheet was firstly synthesized by extracting the Al layer from Ti_3AlC_2-MAX phase, then intercalated by LiCl to get monolayer MXene (Figure S6, Supporting Information). The obtained few-layer MXene was then modified by DCTES to graft the –$C_{12}H_{26}$ group on the surface of MXene nanosheets (Figure S7, Supporting Information). Figure 5e shows the TEM image of the surface-grafted MXene nanosheet. In Figure 5d, the characteristic peaks of DCTES-MXene at 3435 and 1632 cm^{-1} were from the vibrations of the $Ti_3C_2T_x$ surface end groups –OH and C–O, respectively. In addition, the asymmetric and symmetric stretching vibrational peaks of C–H bonds (2973, 2920, and 2849 cm^{-1}), C–Si bonds (1467 and 1388 cm^{-1}) and O–Si bonds (1166, 1103, and 1078 cm^{-1}) on DCTES

© 2023 Wiley-VCH GmbH

2365709x, 2023, 15, Downloaded from https://onlinelibrary.wiley.com/doi/10.1002/admt.202300157 by du fu - Columbia University Libraries , Wiley Online Library on [07/09/2023]. See the Terms and Conditions (https://onlinelibrary.wiley.com/terms-and-conditions) on Wiley Online Library for rules of use; OA articles are governed by the applicable Creative Commons License

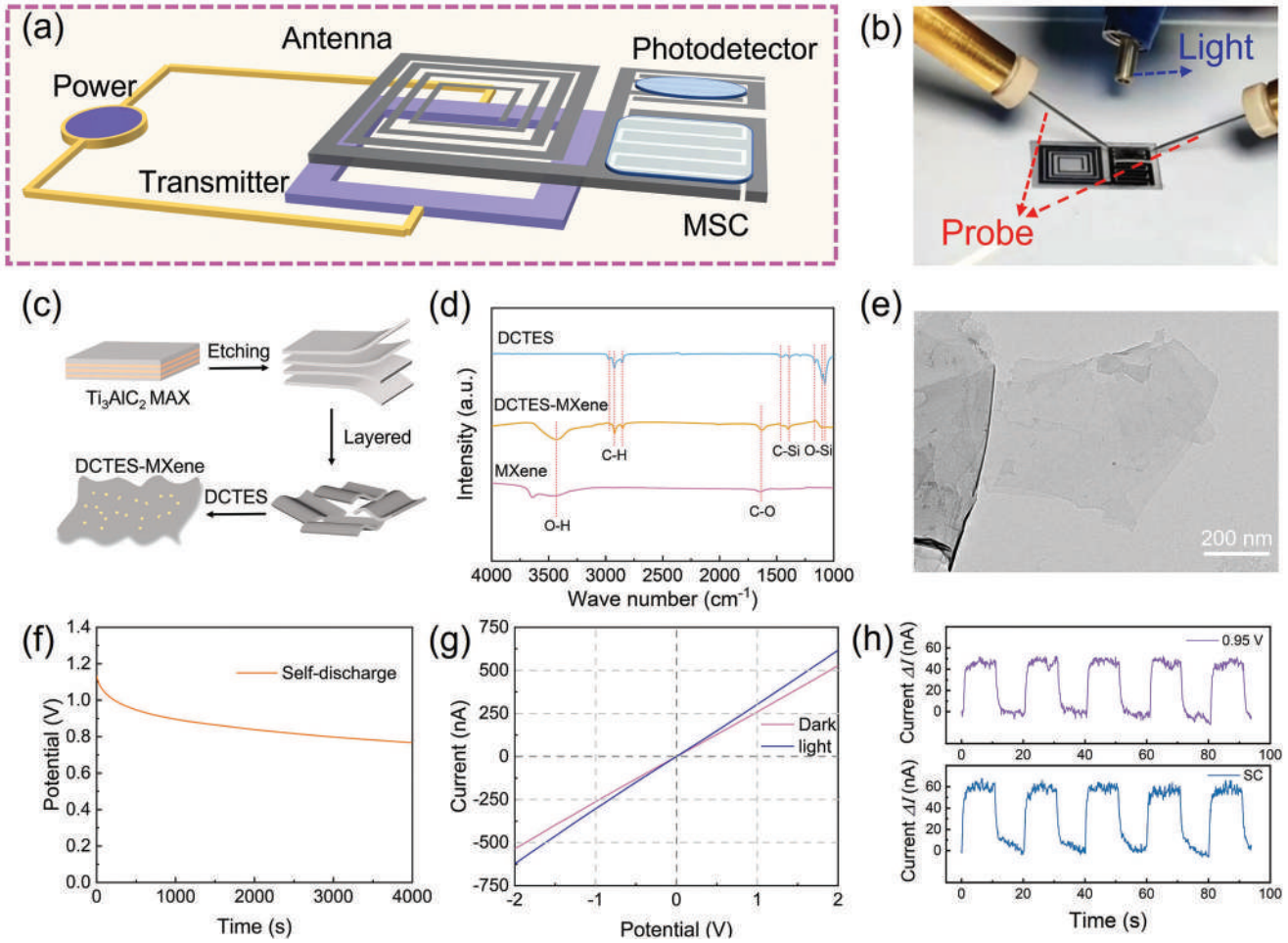

Figure 5. Performance characterization of the integrated device. a) Schematic diagram of device operation. b) Schematic diagram for testing the photodetection performance of integrated devices, showing the photodetector powered by an external power supply. c) Flow chart of DCTES-MXene preparation. d) FTIR spectrum of $Ti_3C_2T_x$ MXene, DCTES-MXene, and DCTES. e) TEM image of the DCTES-MXene nanosheet. f) The self-discharge profile of the optimized Zn-ion MSC. g) The *I–V* characteristic curves of the DCTES-MXene-based photodetector under light and dark states. h) The photoresponse curves of DCTES-MXene based photodetectors driven by MSC and 0.95 V under 808 nm light stimulation, respectively.

molecules were reflected on DCTES-MXene, which proved the successful grafting of DCTES molecules on $Ti_3C_2T_x$.

The photodetection performance of the DCTES-MXene based photodetector in the integrated system was investigated and the corresponding results were also depicted in Figure 5. The self-discharge profile of the supercapacitor in Figure 5f showed that optimized MSC can remain above 0.8 V for 4000 s after being sufficiently charged, indicating a possibility to drive a photodetector for a long period. Figure 5g presents the *I–V* characteristic curves of the DCTES-MXene-based photodetector under light and dark states, respectively. The obvious increase in current under light irradiation showed the obvious photoresponse of the DCTES-MXene device. In order to verify the feasibility and stability of using MSC to drive the photodetector, Figure 5h compares the photoresponse curves of the DCTES-MXene-based photodetector under 808 nm light stimulation. The photocurrent was excited and shut down sequentially with the alternating lighting switches. Similar photoresponse curves, driven by MSC and 0.95 V external bias power supply, respectively, demonstrated a comparable performance of the integrated system with the external power-driven system. Therefore, it was feasible and stable to use an internally integrated MSC instead of an external power supply to drive photodetectors.

3. Conclusion

In summary, an on-chip all-MXene seamlessly multifunctional system with integrated energy harvesting, energy storage, and sensing was successfully fabricated using a one-step laser scribing technology. The three modules in the system were ingeniously integrated into an area of only 1.78 cm^2, including a MXene WCC, a MXene zinc-ion MSC, and a DCTES-MXene photodetector. The coil prepared by MXene was used as a receiver for contactless energy transmission. The received energy by the WCC was subsequently stored in the MSC and used as a power supply to drive the photodetector. Besides, the integrated system was able to be fully charged within 2 min and maintain 90% of its capacity after 100 wireless charging/galvanostatic discharging cycles. The successful demonstration of the on-chip integrated system revealed that the one-step laser scribing strategy not only

© 2023 Wiley-VCH GmbH

2365709x, 2023, 15, Downloaded from https://onlinelibrary.wiley.com/doi/10.1002/admt.202300157 by du fu - Columbia University Libraries , Wiley Online Library on [07/09/2023]. See the Terms and Conditions (https://onlinelibrary.wiley.com/terms-and-conditions) on Wiley Online Library for rules of use; OA articles are governed by the applicable Creative Commons License

inspired the designs of integrated systems but also showed the enormous application potential for flexible integrated systems like IoTs, intelligent healthcare, environment monitoring, etc.

4. Experimental Section

Materials: Ti_3AlC_2-MAX was obtained from Carbon-Ukraine. Hydrofluoric acid (HF, 40%), hydrochloric acid (HCl, 9 M), ammonium solution ($NH_3{\cdot}H_2O$, 30%), zinc chloride ($ZnCl_2$, 99%), and polyvinyl alcohol (PVA; MW = 70 000—100 000) were procured from Aladdin Industrial Inc. Lithium chloride (LiCl, 99%) And dodecyl triethoxysilane (DCTES, 95%) were provided by Macklin Biochemical Co., Ltd. All chemicals were of analytical grade and used directly without further purification. Deionized water was used throughout the all experiment.

Preparation of $Ti_3C_2T_x$ MXene: The MXene was prepared using the selective etching method. Briefly, 1.5 g of Ti_3AlC_2 MAX phase was slowly added into a mixture of 13.5 mL deionized water, 13.5 mL HCl, and 3 mL HF, and stirred at 35 °C for 24 h. Then, the obtained sediment was washed with DI water for several times by centrifugation until the pH of the supernatant reached to natural. The sediment was then collected and dried at 80 °C for 12 h under vacuum to obtain multilayer $Ti_3C_2T_x$ MXene. Subsequently, 1 g of multilayer $Ti_3C_2T_x$ MXene and 1.5 g of LiCl were added into 15 mL DI water under vigorous stirring at room temperature for 12 h to delaminate. After the resulting mixture was shaken by hands and washed with DI water for several times, the supernatant was collected by centrifugation (3500 rpm for 5 min) to obtain monolayer MXene with large size. And the small-sized MXene was obtained after ultrasonication treatment.

Preparation of DCTES-MXene: The DCTES-MXene was synthesized according to the reported literature. $Ti_3C_2T_x$ (0.1 g) was added into the mixture of DI water (1 mL), ethanol (16 mL), and ammonium solution (1.5 mL) with stirring at room temperature for 24 h. Then, 0.1 mL DCTES was added into the mixed solution and vigorous stirring for 24 h. Finally, the DCTES-modified $Ti_3C_2T_x$ was purified by centrifugation and followed dried at 40 °C for 12 h, which was credited as DCTES-MXene.

Preparation of Gel Electrolyte: The PVA/$ZnCl_2$ gel electrolyte was prepared following the method reported in the literature. 3 g of PVA and 6 M $ZnCl_2$ were dissolved into 30 mL DI water with vigorous stirring at 85 °C until the solution became clear.

Fabrication of Integrated Devices: Firstly, a cleaned PET substrate was treated with plasma cleaner to enhance its hydrophilicity. Secondly, the large-sized $Ti_3C_2T_x$ suspension (2 mg mL^{-1}) was spread on the treated PET substrate and dried at 60 °C for 30 min under vacuum. Then, an additional small-sized $Ti_3C_2T_x$ suspension (2 mg mL^{-1}) was dropped on the MSC areal and dried at the same condition. After that, the patterned electrodes were prepared by laser scribing (Power, 20 W). Finally, the PVA/$ZnCl_2$ gel electrolyte and DCES-MXene were coated on the integrated electrodes separately.

Characterization: The X-ray diffraction (XRD) patterns were collected on Rigaku D/Max-2550. The scanning electron microscopy (SEM) images were collected using a NANOSEM 650-6700F microscope. The transmission electron microscopy (TEM) images were taken on a JEOLJEM-2010HT. The electrochemical performance was measured by CHI 760D electrochemical workstations. The photoresponse curves was recorded by Keysight B1500A. The dynamic light scattering was recording by Zetasizer Nano ZS90. The Fourier transform infrared spectroscopy (FTIR) Spectrum Tested by FTIR-650S.

Calculation: The specific areal capacitances (C_A) can be calculated from the cyclic voltammetry curves by the equation

$$C_A = \frac{\int_0^v I dv}{S \Delta V A} \tag{1}$$

where I represents the current, S stands for the scan rate, ΔV is the potential in the CV curve, and A is the areal of the devices. The energy density and power density of the device were obtained from the equations

$$E = C_A \times \Delta V^2 / 7200 \tag{2}$$

$$P = E \times 3600 / \Delta t \tag{3}$$

where E represents the energy density (Wh cm^{-2}), P is the power density (W cm^{-2}), and Δt is the total discharge time.

Supporting Information

Supporting Information is available from the Wiley Online Library or from the author.

Acknowledgements

This work was supported by the National Natural Science Foundation of China (61888102, 62004187) and Beijing Institute of Technology Research Found Program for Young Scholars.

Conflict of Interest

The authors declare no conflict of interest.

Data Availability Statement

The data that support the findings of this study are available from the corresponding author upon reasonable request.

Keywords

all-MXene devices, micro-supercapacitors, photodetectors, wireless charge coils

Received: February 8, 2023
Revised: February 23, 2023
Published online: April 4, 2023

[1] W. Deng, Y. Zhou, A. Libanori, G. Chen, W. Yang, J. Chen, *Chem. Soc. Rev.* **2022**, *51*, 3380.
[2] C. Zhang, T. Bu, J. Zhao, G. Liu, H. Yang, Z. L. Wang, *Adv. Funct. Mater.* **2019**, *29*, 1808114.
[3] Z. Lou, L. Li, L. Wang, G. Shen, *Small* **2017**, *13*, 1701791.
[4] Y.-G. Park, S. Lee, J.-U. Park, *Sensors* **2019**, *19*, 4353.
[5] C. Ma, M. Ma, C. Si, X. Ji, P. Wan, *Adv. Funct. Mater.* **2021**, *31*, 2009524.
[6] X. Chen, Z. Hou, G. Li, W. Yu, Y. Xue, G. Niu, M. Xin, L. Yang, C. Meng, S. Guo, *Nano Energy* **2022**, *101*, 107606.
[7] S. Zheng, H. Wang, P. Das, Y. Zhang, Y. Cao, J. Ma, S. (Frank) Liu, Z.-S. Wu, *Adv. Mater.* **2021**, *33*, 2005449.
[8] C. S. Kim, H. M. Yang, J. Lee, G. S. Lee, H. Choi, Y. J. Kim, S. H. Lim, S. H. Cho, B. J. Cho, *ACS Energy Lett.* **2018**, *3*, 501.
[9] C. Yang, Q. Wu, J. Liu, J. Mo, X. Li, C. Yang, Z. Liu, J. Yang, L. Jiang, W. Chen, H. Chen, J. Wang, X. Xie, *Nat. Commun.* **2022**, *13*, 2556.
[10] J. Kim, P. Gutruf, A. M. Chiarelli, S. Y. Heo, K. Cho, Z. Xie, A. Banks, S. Han, K. Jang, J. W. Lee, K. Lee, X. Feng, Y. Huang, M. Fabiani, G. Gratton, U. Paik, J. A. Rogers, *Adv. Funct. Mater.* **2017**, *27*, 1604373.
[11] Y. Yue, Z. Yang, N. Liu, W. Liu, H. Zhang, Y. Ma, C. Yang, J. Su, L. Li, F. Long, Z. Zou, Y. Gao, *ACS Nano* **2016**, *10*, 11249.
[12] J. Park, D. B. Ahn, J. Kim, E. Cha, B.-S. Bae, S.-Y. Lee, J.-U. Park, *Sci. Adv.* **2019**, *5*, eaay0764.
[13] A. Saleh, S. Wustoni, E. Bihar, J. K. El-Demellawi, Y. Zhang, A. Hama, V. Druet, A. Yudhanto, G. Lubineau, H. N. Alshareef, S. Inal, *J. Phys. Mater.* **2020**, *3*, 044004.

© 2023 Wiley-VCH GmbH

2365709x, 2023, 15, Downloaded from https://onlinelibrary.wiley.com/doi/10.1002/admt.202300157 by du fu - Columbia University Libraries , Wiley Online Library on [07/09/2023]. See the Terms and Conditions (https://onlinelibrary.wiley.com/terms-and-conditions) on Wiley Online Library for rules of use; OA articles are governed by the applicable Creative Commons License

[14] P. Li, N. Su, Z. Wang, J. Qiu, *ACS Nano* **2021**, *15*, 16811.
[15] M. Shen, W. Jiang, K. Liang, S. Zhao, R. Tang, L. Zhang, J. Wang, *Angew. Chem.* **2021**, *133*, 27219.
[16] M. Naguib, M. Kurtoglu, V. Presser, J. Lu, J. Niu, M. Heon, L. Hultman, Y. Gogotsi, M. W. Barsoum, *Adv. Mater.* **2011**, *23*, 4248.
[17] G. Ma, H. Shao, J. Xu, Y. Liu, Q. Huang, P.-L. Taberna, P. Simon, Z. Lin, *Nat. Commun.* **2021**, *12*, 5085.
[18] X. Zhan, C. Si, J. Zhou, Z. Sun, *Nanoscale Horiz.* **2020**, *5*, 235.
[19] N. Chen, Y. Zhou, S. Zhang, H. Huang, C. (John) Zhang, X. Zheng, X. Chu, H. Zhang, W. Yang, J. Chen, *Nano Energy* **2021**, *85*, 106007.
[20] M. Han, Y. Liu, R. Rakhmanov, C. Israel, M. A. S. Tajin, G. Friedman, V. Volman, A. Hoorfar, K. R. Dandekar, Y. Gogotsi, *Adv. Mater.* **2021**, *33*, 2003225.
[21] Y. Shao, L. Wei, X. Wu, C. Jiang, Y. Yao, B. Peng, H. Chen, J. Huangfu, Y. Ying, C. J. Zhang, J. Ping, *Nat. Commun.* **2022**, *13*, 3223.
[22] S. Guo, K. Wu, C. Li, H. Wang, Z. Sun, D. Xi, S. Zhang, W. Ding, M. E. Zaghloul, C. Wang, F. A. Castro, D. Yang, Y. Zhao, *Matter* **2021**, *4*, 969.
[23] L. Li, W. Liu, K. Jiang, D. Chen, F. Qu, G. Shen, *Nano–Micro Lett.* **2021**, *13*, 100.
[24] Y.-Y. Peng, B. Akuzum, N. Kurra, M.-Q. Zhao, M. Alhabeb, B. Anasori, E. C. Kumbur, H. N. Alshareef, M.-D. Ger, Y. Gogotsi, *Energy Environ. Sci.* **2016**, *9*, 2847.
[25] H. Hu, T. Hua, *J. Mater. Chem. A* **2017**, *5*, 19639.
[26] L. Hao, H. Zhang, X. Wu, J. Zhang, J. Wang, Y. Li, *Composites, Part A* **2017**, *100*, 139.
[27] N. R. Hemanth, B. Kandasubramanian, *Chem. Eng. J.* **2020**, *392*, 123678.
[28] H. Huang, X. Chu, Y. Xie, B. Zhang, Z. Wang, Z. Duan, N. Chen, Z. Xu, H. Zhang, W. Yang, *ACS Nano* **2022**, *16*, 3776.
[29] N. Wang, J. Liu, Y. Zhao, M. Hu, R. Qin, G. Shan, *ChemNanoMat* **2019**, *5*, 658.
[30] S. K. Cheah, E. Perre, M. Rooth, M. Fondell, A. Hårsta, L. Nyholm, M. Boman, T. Gustafsson, J. Lu, P. Simon, K. Edström, *Nano Lett.* **2009**, *9*, 3230.
[31] C. J. Zhang, M. P. Kremer, A. Seral-Ascaso, S.-H. Park, N. McEvoy, B. Anasori, Y. Gogotsi, V. Nicolosi, *Adv. Funct. Mater.* **2018**, *28*, 1705506.
[32] Y. Liu, J. Yu, D. Guo, Z. Li, Y. Su, *J. Alloys Compd.* **2020**, *815*, 152403.
[33] A. Scidà, S. Haque, E. Treossi, A. Robinson, S. Smerzi, S. Ravesi, S. Borini, V. Palermo, *Mater. Today* **2018**, *21*, 223.
[34] C. Gao, J. Huang, Y. Xiao, G. Zhang, C. Dai, Z. Li, Y. Zhao, L. Jiang, L. Qu, *Nat. Commun.* **2021**, *12*, 2647.

© 2023 Wiley-VCH GmbH

2365709x, 2023, 15, Downloaded from https://onlinelibrary.wiley.com/doi/10.1002/admt.202300157 by du fu - Columbia University Libraries , Wiley Online Library on [07/09/2023]. See the Terms and Conditions (https://onlinelibrary.wiley.com/terms-and-conditions) on Wiley Online Library for rules of use; OA articles are governed by the applicable Creative Commons License